Observed Relationship Between BRF Spectral-Continuum Variance and Macroscopic Roughness of Clay Sediments

Gregory Badura, Charles M. Bachmann, *Senior Member, IEEE*, Justin Harms, and Andrei Abelev

***Abstract*— Spectral data offer a means of estimating the critical parameters of sediments, including sediment composition, moisture content, surface roughness, density, and grain-size distribution. Macroscopic surface roughness in particular has a substantial impact on the structure of the bidirectional reflectance factor (BRF) and the angular distribution of scattered light. In developing the models to invert the properties of the surface beyond just surface composition, roughness must also be accounted for in order to achieve reliable and repeatable results. This paper outlines laboratory studies in which the BRF and surface digital elevation measurements were performed on dry clay sediments. The results were used to explore the suitability of various roughness metrics to account for the radiometric effect of surface roughness. The metrics that are specifically addressed in this paper include random roughness and sill variance. Relative accuracy and tradeoffs between these metrics are described. We find that spectral variability, especially near spectral absorption features, correlates strongly with the quantified measures of surface roughness. We also find that spectral variability is sensitive to the sensor fore-optic size. The results suggest that roughness parameters might be directly determined from the spectrum itself. The relationship between spectral variability and macroscopic surface roughness was particularly strong in some broad spectral ranges of the visible, near infrared, and shortwave infrared, including the near-infrared region between 600 and 850 nm.**

***Index Terms*— Bidirectional reflectance factor (BRF), digital elevation model (DEM), goniometer of the Rochester Institute of Technology-two (GRIT-T), roughness, sediment.**

Manuscript received September 18, 2018; revised November 5, 2018, January 9, 2019 and February 24, 2019; accepted March 13, 2019. Date of publication April 22, 2019; date of current version August 27, 2019. This research is funded by an academic grant from the National Geospatial-Intelligence Agency (Award No. #HM0476- 17-1-2001, Project Title: Hyperspectral Video Imaging and Mapping of Littoral Conditions), approved for public release 18-087, in part by the Naval Research Laboratory under Award N00173-15-1-G904 and in part by the Frederick and Anna B. Wiedman Professorship in Imaging Science at the Rochester Institute of Technology. *(Corresponding author: Gregory Badura.)*

G. Badura was with the Chester F. Carlson Center for Imaging Science, Rochester Institute of Technology, Rochester, NY 14623 USA. He is now with the Georgia Tech Research Institute (GTRI), Atlanta, GA 30318 USA (e-mail: gpb6751@rit.edu).

C. M. Bachmann is with the Chester F. Carlson Center for Imaging Science, Rochester Institute of Technology, Rochester, NY 14623 USA.

J. Harms was with the Chester F. Carlson Center for Imaging Science, Rochester Institute of Technology, Rochester, NY 14623 USA. He is now with the United States Air Force, Washington, DC USA.

A. Abelev is with the U.S. Naval Research Laboratory, Marine Geosciences Division, Washington, DC 20375 USA.

Color versions of one or more of the figures in this article are available online at http://ieeexplore.ieee.org.

Digital Object Identifier 10.1109/TGRS.2019.2908170

I. Introduction

THE role of macroscopic roughness in the directional reflectance of a particulate medium is sensitive to scales ranging from the size of an individual particle to the field of view of an airborne sensor [1]. While all scales of roughness ultimately play a role in the directional reflectance of a surface, several studies have shown that the macroscopic surface roughness on the scale of a single particle to the scale of a centimeter is considered sufficient to explain the photometric roughness [2]–[4]. When attempting to retrieve geophysical parameters from remotely sensed imagery, failing to account for surface roughness ignores important reflectance phenomena, such as multiple scattering and shadowing within surface cavities. For example, Wang *et al.* [5] employed an image-based approach which used the bidirectional reflectance factor (BRF) to analyze the effect of illumination zenith angle on both the rough and smooth soil surfaces. They found that the BRF images of clay loam surfaces consisting of large clods were largely made up of shaded pixels, whereas the BRF images of smooth soil surfaces were dominated by illuminated pixels [5]. In another study, Shepard and Helfenstein [3] found that as surface microstructures of soils were gradually removed by mechanical compression, reflectance ultimately became more isotropic and eventually exhibited stronger forward scattering. Other recent studies comparing rough and smooth areas of beach sediments on the Queensland coast of Australia have shown the same trend [6].

Given the experimental results mentioned earlier, it is clearly necessary to account for spectral phenomena due to centimeter-scale correlations in surface roughness when examining directional reflectance measurements. Techniques for correlating surface roughness metrics on a centimeter scale with directional reflectance measurements have shown promising results. Croft *et al.* [7], [8] obtained point laser data at 2-mm sample spacing for several soil types and utilized the geostatistical approach of kriging to characterize spatially distributed surface roughness. They found that there was a strong correlation between the ratio of forward-scattered to backscattered hemispherical conical reflectance factors (HCRFs) in the principal plane and a metric of roughness known as sill variance across multiple different soil types [7], [8]. While these studies show promise for the use of centimeter-scale digital elevation models (DEMs) in determining the directional reflectance of sediments, these

studies did not include a detailed analysis of the relationship between spectrally dependent BRF measurements and macroscopic roughness, particularly in the regions of absorption features. This paper aims to address this gap by extending the approaches used in the previous studies and also utilizing novel metrics of spectral band variance as a function of roughness.

It is well documented that the depths of absorption features provide information regarding the relative abundance of minerals within soils [9]–[11]. While examining the band depths of absorption features can be a useful tool in remote-sensing studies, the approach can be complicated by nonlinear scattering effects that cause uncertainties in both the band center and the band shape. The absorption band shape can also change drastically depending on the factors, such as the path length traveled through a soil medium and the wavelength-dependent absorption coefficient [10]. Depending on these factors, the absorption feature can take on three different forms: a Gaussian shape, a flat-bottomed shape due to saturation, and a doublet shape with two absorption maxima [10], [12].

The relative orientations of the sensor and illumination source can also have drastic effects on the manifestation of spectral absorption features. Hapke [1] noted that the band depth is highly dependent on the sensor and the illumination geometry. If the directional reflectance of a material is measured with the sensor and illumination sources close to nadir, then multiple scattering will significantly increase the wings of absorption bands [1]. However, if the reflectance is measured while either the illumination source or the sensor is oriented at an oblique angle, then the surface reflectance is dominated by single scattering which results in a shallower absorption depth [10]. This conclusion is supported by the evidence from another study by Huguenin and Jones [12], who noted that varying the phase angle can result in changes in the extent of shadowing due to the macroscopic surface roughness, which produces significant shifts in the apparent centers, widths, and strengths of absorption bands.

In addition to physical parameters that influence the properties of absorption bands, sensor limitations can also influence the statistical analysis of band shapes. Factors such as low albedo of the sample or shadowing due to roughness can lead to lower signal-to-noise ratios at certain sensor-illumination geometries. In the cases with a low signal-to-noise ratio, it can be difficult to differentiate absorption bands from sensor noise. This can lead to bands being shifted from their actual positions, or being overlooked entirely [12]. Increasing the intensity of the light source and increasing the number of reflectance measurements sampled at each sensor orientation are ways to mitigate this, but noise sources, such as the shot noise, are an inherent limitation when measuring reflectance using both the spectrometers and imaging sensors [12], [13].

The goals of the experiments described in this paper are to: 1) analyze spectral phenomena resulting from macroscopic surface roughness using directional BRF measurements and 2) determine if the observed spectral phenomena have a dependence on the sensor field-of-view. Understanding these relationships is important for the retrieval of geophysical parameters from spectral measurements. Our results could be useful for describing the empirical relationship between spectral reflection properties and soil physical properties, such as grain-size distribution and macroscopic roughness. This is important because typical sediment surfaces exhibit roughness on multiple scales, meaning that failure to account for roughness can complicate efforts to retrieve geophysical parameters from soil spectral measurements.

Fig. 1. (Left) GRIT-T in the laboratory setting with sample in holder. (Right) GRIT-T in a field setting.

II. Methods

A. Goniometer of the Rochester Institute of Technology-Two: Hyperspectral BRF and DEM Measurement Capabilities

A novel goniometer system capable of obtaining very high accuracy BRF measurements of vegetation and soils was recently developed in the Chester F. Carlson Center for Imaging Science, Rochester Institute of Technology [14], [15], known as the goniometer of the Rochester Institute of Technology-two (GRIT-T). The GRIT-T provides an important tool for studying the surface materials, such as sediments and the impact of their geophysical properties on spectral BRF. A number of important surface properties, including surface roughness, grain-size distributions, and fill factor, are all known to contribute to the observed angular dependence of the spectral BRF [10]. Past studies have included spectroscopic and BRDF studies of grain size [16]–[19], fill factor [20], [21], and surface roughness [22], and the properties, such as grain size, for example, play an important role in environmental processes, such as desertification [23] and soil erosion [24]–[26]. Ben-Dor *et al.* [27] provided a review of the role of spectroscopy in soil environmental applications.

The GRIT-T integrates a dual-view design using two analytical spectral devices (ASDs) FR4 spectroradiometers to capture target-reflected radiance, as well as downwelling sky radiance. The two spectroradiometers record spectral radiance in the spectral range between 350 and 2500 nm, covering the visible and near infrared (VNIR) as well as shortwave infrared (SWIR) at 1-nm spectral intervals. The system was designed to be highly accurate within both field and laboratory settings.

An onboard laser measurement unit allows the GRIT-T to determine true distance to the target surface from nadir. This information can be used in conjunction with a rotating sensor head to track the same position on the ground, thus mitigating parallax effects that would ordinarily be present when the target plane and the surface do not coincide.

The system is designed using an automatic leveling technology to obtain BRF measurements on a rough terrain while still maintaining true angular measurements with respect to the target within 0.2°. The GRIT-T also incorporates an onboard GPS IMU system which provides information about the orientation and position of the system, as well as the knowledge of the Sun's position through the GPS timestamp. The system also features an open frame design, combined with a small-profile rotating arm, which allows for the device to accurately measure a target while minimizing self-shading in and near the principal plane of the light source.

The surface roughness models of the target, in the form of DEMs, are produced by combining laser range finder measurements with GRIT-T's precision movement capabilities. The elevation information provides multiple benefits for the BRF analysis, including the determination of overall surface slope and the ability to analyze macroscopic roughness effects on light scattering. The on-board laser distance unit utilizes triangulation with a 650-nm laser beam in order to measure overall distance to the target. Laboratory tests showed that the sensor has an elevation measurement repeatability within 0.5 mm and an elevation measurement accuracy within 2 mm. It was shown that the laser sensor has an elliptical beam spot size of approximately 11 mm $\times$ 4.5 mm when operating at a typical target-to-sensor distance of 600 mm [14], [15].

Due to the fact that the on-board laser sensor obtains only a single distance measurement at a time, the laser sensor must be positioned by the goniometer in order to sample elevation measurements within the target area. A consequence of this mode of operation is that any errors in mechanical motions will translate to positioning inaccuracy in the DEM. In addition, errors in the machining of the optical system of the laser sensor unit must be compensated for in order to achieve a reasonable DEM. Postprocessing tools have been developed to compensate for these errors. Laboratory calibration tests show that the average error between the center of an alignment laser aligned with the optical axis and the center of the intended target is 3.6 mm. Therefore, in order to mitigate positional errors when producing DEMs, we limit our sampling density to roughly 1 pt/cm^2.

B. Laboratory Measurement Procedure

The sediment samples used in this experiment originally had high soil moisture content when collected during a field experiment in northwestern Nevada. Prior to beginning the experiments, the samples were dried in an oven at 110 $^\circ C$ for at least 24 h in order to remove all moisture contents. These samples were mechanically pulverized into "clods" of random shapes and sizes. The dried samples then underwent a sieve analysis in order to determine the grain-size distribution of the sample; based on this analysis, it was determined that, on average, the "clods" were approximately 10 mm in size when in this initial state. The sample was then placed in a sample holder with a depth of approximately 3 in and a diameter of 10 in. This sample holder was then covered and shaken mechanically for 2 min, with the goal of creating a random distribution of the constituent grains of the material. After performing this shaking process, the side of the sample holder was tapped in order to induce settling of the material, in such a manner that the orientation of the microfacets would not change in between BRF measurements.

BRF scans were then performed to obtain the reflectance of the material as a function of viewing azimuth and zenith angles for each illumination geometry. A total of four hyperspectral BRF scans were performed for each sample and illumination geometry and for each sensor fore-optic of the spectrometer used. The chosen fore-optics used in this paper were 5° and 8°. The experiments were repeated for the illumination zenith angles of 25° and 45°. Hyperspectral BRF measurements were obtained for viewing the zenith angles between -65° and $+65^\circ$ over the full 360° azimuthal sampling of GRIT-T [15]. The sampling resolution for the BRF measurements was 10° in zenith and 12° in azimuth. In order to achieve a high signal-to-noise ratio, 80 spectral radiance measurements were averaged at each position along the scan pattern. The distance from the fore-optic to the target plane at nadir was $\sim$55 cm, which results in a projected FOV on the surface of $\sim$18 cm^2, when using the narrower 5° attachment. At the most extreme sensor zenith angles of 65°, the projected FOV onto the surface takes on an elliptical area of $\sim$ 42 cm^2. Using an irradiance meter, we verified that the irradiance from our collimated light source at the edges of this projected FOV area was constant to within 2%.

A grain-size distribution analysis was performed on all of the samples in this paper by using mesh sieves and a Humboldt sieve shaker to mechanically separate the clods and particles by diameter. The results of performing this analysis on the roughest samples (the R1 samples) revealed that $\sim$90% of the clods of the R1 samples had a diameter that was greater than 0.5 cm. By examining the DEMs developed from the samples in this paper and the overhead images, we can reasonably assume that the largest clods are approximately ellipsoidal with a semiminor diameter of 1 cm and a semimajor diameter of 1.5 cm. This gives a ground projected area for the largest clods of 4.7 cm^2. Fig. 2 shows that there is very little interclod separation due to the fact that our samples were randomly shaken during sample preparation.

Considering the above discussion, we can see that a single clod would only occupy at most $\sim$26% of the field of view when the sensor fore-optic is at nadir and $\sim$11% of the field of view when the sensor fore-optic is at an extreme zenith angle. Because the field-of-view area is so much larger than the projected area of the largest clods and their typical separation, we could assume that roughness would be constant across the varying size of the field-of-view area with the angle.

We note that we use the term BRF to indicate that our spectral measurements estimate the ratio of the reflected radiant flux from a uniform surface area to the reflected radiant flux from an ideal and diffuse surface of the same area [28]–[30]. The ideal diffuse surface is approximated in our laboratory measurements by a Spectralon calibration panel. Other researchers have distinguished between BRF, which is an idealized concept, and the practical implementation of BRF estimates, which involve both a sensor field-of-view and source extent that are finite; the term biconical reflectance

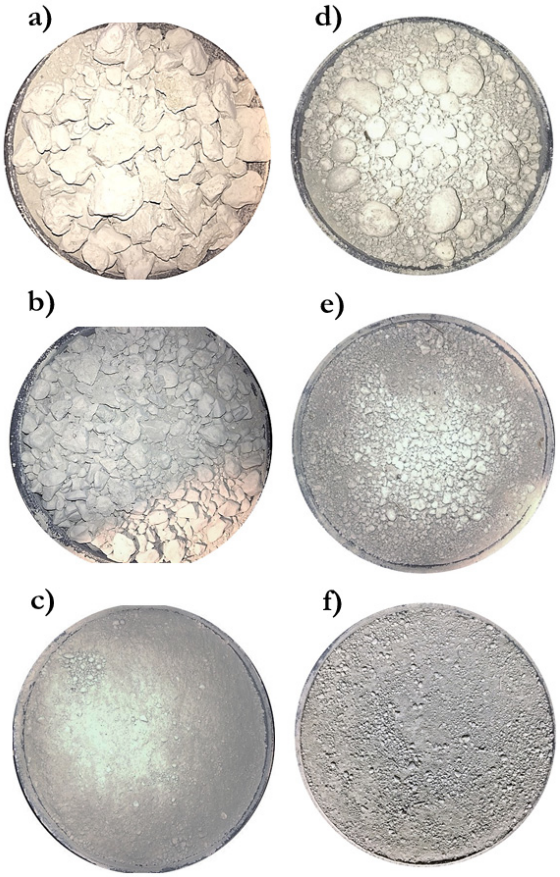

Fig. 2. Images of the sample within the sample holder for the different roughness states of the materials. (a)–(c) Sample WA02-03 and (d)–(f) sample WA04-02 at roughness levels R1, R2, and R3, respectively.

factor (BCRF) is often used to describe this practical implementation [8], [29]. The term BCRF would also be acceptable to describe our laboratory measurement scheme; however, we use the term BRF in this paper with the understanding that we estimate this idealized quantity with a practical measurement.

In addition to obtaining BRF measurements, digital elevation measurements of the sample were obtained at a sampling density of approximately 1 pt/cm^2 using the GRIT-T's laser distance measuring unit.

After performing a series of scans for a given roughness level of the sample, the material was pulverized in order to create a new sample made up of the same sediment, but with its grain-size distribution shifted toward smaller grain sizes. For each roughness state, the same series of BRF scans and DEM measurements were then repeated. This cycle of sample preparation and radiometric analysis was repeated a total of three times for each sample, providing a total of three different roughness levels for each sediment sample in this paper. In this way, the reflectance of the same material with different levels of roughness could be compared, and roughness metrics could be computed for each state from the corresponding digital elevation measurements. In this paper, we used two soil samples denoted "WA02-03" and "WA04-02." We show the overhead images of these samples in Fig. 2 for the different roughness states used in this paper. The BRF measurements of sample WA02-03, obtained when the light source was oriented at the zenith angles of 25° and 45° and a 5° spectrometer fore-optic attachment was used, are shown in Fig. 3.

C. Roughnesss Metrics Considered in This Study

1) Semivariogram Modeling: Heterogeneous materials such as soils are composed of grains of varying size, shapes, and composition. Because of the heterogeneous nature of a macroscopically rough surface, it is appropriate to model the elevation of the surface as a random variable $Z(x)$, where x is the spatial coordinate of the surface, and Z is the elevation

$$Z(x) = \mu + \epsilon(x). \tag{1}$$

In (1), μ is the mean elevation and $\epsilon(x)$ is a stochastic component of surface elevation. If it is also assumed that the random variable is an intrinsic random function (IRF), then the random variable satisfies the following relationships for the separation or lag, h, between two spatial locations:

$$m(h) = E\left[Z(x+h) - Z(x)\right] \tag{2}$$

$$\Upsilon(h) = \frac{1}{2}\mathrm{var}\left[Z(x+h) - Z(x)\right] \tag{3}$$

where $m(h)$ is the linear drift, and Υ is the theoretical semivariogram. According to Chiles and Delfiners [31], the theoretical semivariogram of the IRF can be related to the covariance function of the process in the following manner:

$$\Upsilon(h) = C(0) - C(h). \tag{4}$$

In (4), $C(0) = \sigma^2$ is the total variance of the random process, defined formally as the semivariogram sill [31].

A critical tool for examining statistical properties of a spatial process is the empirical semivariogram. The empirical semivariogram is defined in (5) [32] as

$$\hat{\Upsilon}(h) = \frac{1}{2N(h)} \sum_{(i,j)\in N(h)} |Z_i - Z_j|^2. \tag{5}$$

In this equation, $N(h)$ denotes the number of pairs of observations whose spatial coordinates s_i, s_j are separated by the lag distance, h. The empirical semivariogram is typically fitted to theoretical semivariograms through least-squares methods [33].

One type of theoretical semivariogram model that is frequently used for modeling soils is the spherical model [8]. This model takes the following form:

$$\Upsilon(h) = \begin{cases} C_0 + C\left(\frac{3h}{2r} - \frac{1}{2}\left(\frac{h}{r}\right)^3\right), & \textbf{for } 0 \le h \le r) \\ C_0 + C, & \textbf{for } h > r \end{cases} \tag{6}$$

where C_0 is the uncorrelated variation at the scale of sampling, and C is the correlated component representing continuity of the semivariogram [34]. Note that $C_0 + C$ represents the sill value. The value r represents the sill range or the lag distance at which the sill is reached. The spherical model is often used to model soil and sand surfaces due to its ability to encapsulate abrupt shifts in elevation [35], [36].

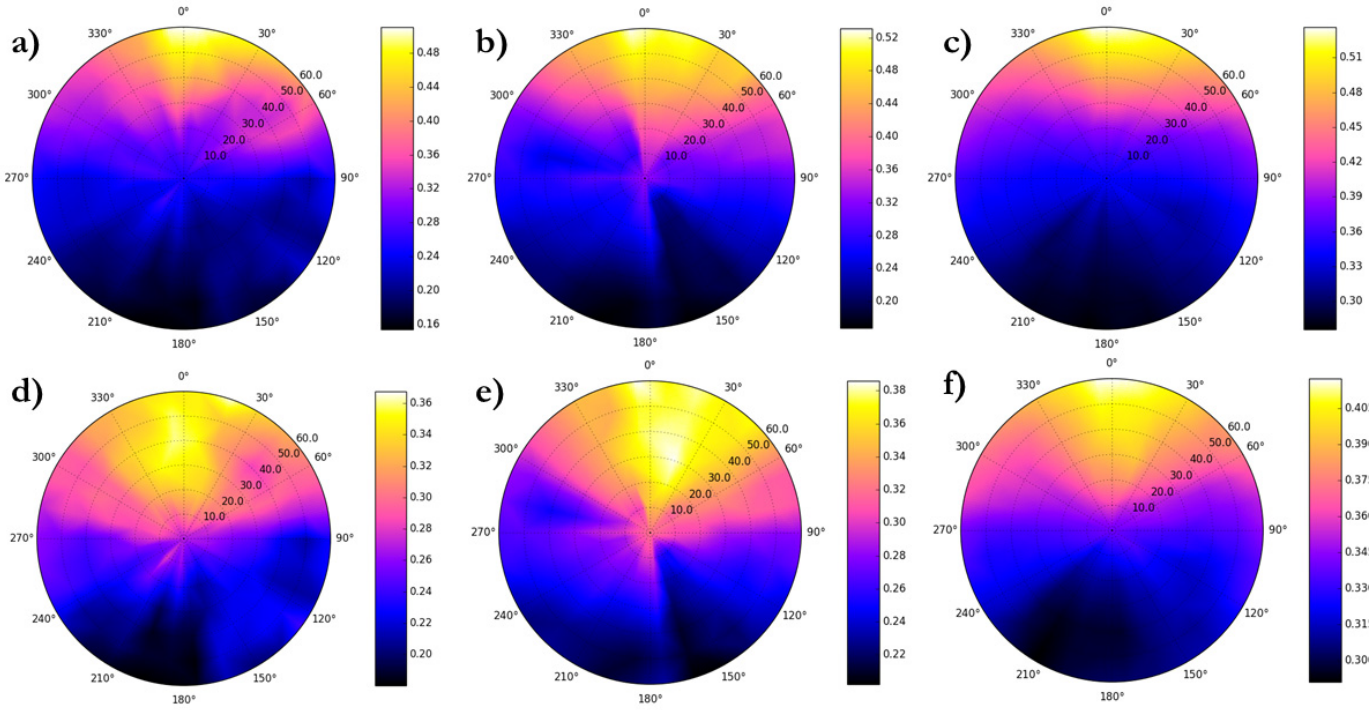

Fig. 3. BRF measurements of the sample within the sample holder for the different roughness states of the materials at 1910 nm. Sample WA02-03 at roughness levels R1, R2, and R3 with the light source oriented at (a)–(c) 45° and (e)–(f) 25°. All used 5° spectrometer fore-optic attachments.

Another theoretical semivariogram model that will be considered in this paper is the exponential model. This model takes on the following form [34]:

$$\Upsilon(h) = \begin{Bmatrix} 0, & \textbf{for } h = 0 \\ C_0 + C[1 - e^{\frac{-h}{r}}], & \textbf{for } h > r \end{Bmatrix}. \tag{7}$$

Several studies have utilized the sill value of the semivariogram as a metric for characterizing the roughness of a randomly distributed soil, since the semivariogram models the distances over which the soil can be considered to be spatially correlated [7], [8]. In the experiments that we describe in this paper, we describe mechanical shaking of the surface prior to measuring BRF in order to satisfy the assumptions necessary for an IRF. In Fig. 4, a GRIT-T DEM data set is postprocessed using interpolation based on ordinary kriging of a soil surface using a spherical semivariogram model. We chose ordinary kriging, because it is derived directly from the empirical semivariogram. This metric is preferable to other interpolation schemes, because it incorporates the random nature of the surface in the interpolation result [33].

2) Random Roughness: The random roughness (RR) is a simple metric that is often used as a baseline measure in many studies on soil roughness [37]. The metric is defined as

$$RR = \sqrt{\frac{1}{N}\sum_{i=1}^{N}(Z_i - \bar{Z})^2} \tag{8}$$

where N is the total number of elevation measurements obtained, Z_i is the ith elevation measurement, and $\bar{Z}$ is the mean elevation. Some disadvantages of the RR metric are that it does not take into account horizontal information about surface roughness, and that it is not derived from any physical model.

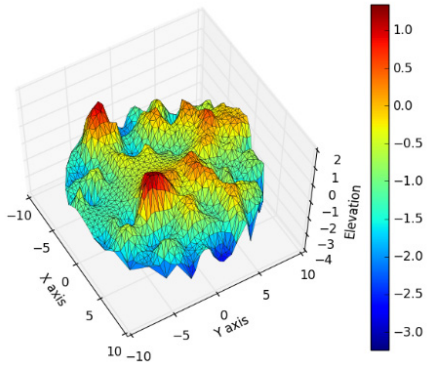

Fig. 4. GRIT-T DEM after performing interpolation using ordinary kriging. Units for the x-axis, y-axis, and elevation-axis are given in centimeters.

D. Spectral Derivatives

In this paper, we obtained numerical derivatives using standard finite approximation methods. Central difference formulas are employed, and approximations are made to within a truncation error of $O(\Delta\lambda^2)$, where $\Delta\lambda$ is the separation between adjacent bands. The first derivative of the spectra S is estimated by

$$S'(\lambda_i) = \frac{S(\lambda_i + \Delta\lambda) - S(\lambda_i - \Delta\lambda)}{2\Delta\lambda} \tag{9}$$

where λ_i is the wavelength at which the first derivative is being estimated. The second derivative can similarly be

approximated by

$$S''(\lambda_i) = \frac{S(\lambda_i + \Delta\lambda) - 2S(\lambda_i) + S(\lambda_i - \Delta\lambda)}{\Delta\lambda^2}. \quad (10)$$

In order to facilitate visual comparison between different orders of derivatives as the value $\Delta\lambda$ increases, higher order derivatives can be "enhanced" by replacing the denominator with the value of $2\Delta\lambda$ [38]. Because this approach enhances the spectral detail of the derivatives, we adopt it in this paper.

In the spectral analysis, noise affects the accuracy of numerical derivatives; however, the impact of noise can be mitigated through the use of smoothing filters. One must use caution when employing smoothing techniques in order to avoid suppressing spectral features in the process of smoothing. For this study, the Savitsky–Golay filter was chosen, since it can resolve relatively weak spectral absorption features [39]. One limitation of using the Savitsky–Golay filter is that noise is assumed constant across the spectrum, while in reality, noise is a function of factors such as signal strength and frequency [13]. We used visual inspection and simple error metrics to determine the success of the filter's noise removal performance without altering identified spectral features.

A critical step in the use of spectral derivatives is the selection of suitable values of $\Delta\lambda$ [38]. Features with widths that are smaller than the chosen value of $\Delta\lambda$ will be undetected by numerical derivatives, while features that are at the scale of $\Delta\lambda$ will be magnified. In this way, one can use the average width of a spectral absorption feature of interest to isolate the relevant features, while also smoothing over noise that is finer than the scale of the feature of interest. A downside of using larger values of $\Delta\lambda$ is that it will not be possible to calculate derivatives near the beginning or ending of the spectrum, due to the fact that central difference formulas are computed at the middle point of a wavelength range [38].

E. Continuum Removal

Clark and Roush [9] first suggested that the continuum of a reflectance spectrum could be removed by dividing it into the reflectance spectrum in order to isolate the absorption features of interest. The continuum of a reflectance spectrum can be found by fitting a convex hull over the local maxima of the reflectance spectra using straight line segments. Calculation of the continuum by means of the convex hull can be performed over the entire reflectance spectrum [40] or over isolated absorption bands of interest by using predetermined wavelengths that straddle the diagnostic feature [41]. Both of these approaches are utilized in this paper. After obtaining the continuum line of the spectrum, the continuum-removed reflectance can be calculated by dividing the original reflectance values by the corresponding value along the continuum line. This process separates the absorption features from the background absorption of the spectrum, allowing them to be more easily compared.

When performing continuum removal on the diagnostic features of interest by fitting the convex hull between predetermined wavelength values, it is straightforward to retrieve the band depth of each point within the absorption feature from the simple relationship

$$D(\lambda) = 1 - S_{CR}(\lambda) \quad (11)$$

where $D(\lambda)$ is the band depth at a given wavelength and $S_{CR}(\lambda)$ is the continuum-removed reflectance spectrum at a given wavelength [41]. By using this relationship, it is possible to analyze how the absorption band properties, such as depths, shapes, and absorption centers, vary with sensor viewing orientation.

In this paper, we perform continuum removal for the BRF measurement at each sensor orientation. In this way, the number of continuum line spectra is equal to the number of measurement directions in the BRF scan pattern. The scan patterns were held constant across all the samples to ensure that the sampling density did not influence the results.

III. Analysis and Results

A. Roughness Metric Retrieval Results

Two metrics of roughness were computed using post-processed DEMs of the GRIT-T laser range measurements. These were the sill value and the random-roughness. In this section, the results of modeling the macroscopic roughness of the study samples using these different metrics are compared and analyzed.

1) Semivariogram Sill Values and Random Roughness: Shown in Table I are the computed values of random roughness using (8). Note again that an increasing roughness level is indicative of increasing smoothness of the material (i.e., the roughness level 1 is the roughest, and the roughness level 3 is the smoothest).

Before calculating experimental semivariograms, the elevation measurements of each DEM scan were examined by the histogram analysis in order to ensure a normal distribution. All data conformed to the criterion that the skewness of the distribution be less than 1 [4]. It was further assumed that the surface was isotropic in slope orientation. As was discussed in Section II, the two theoretical semivariogram models that were considered in this paper were the exponential model and the spherical model. These two models were chosen, because they accurately model short-scale linear trends that are the characteristic of soil clods. Experimental semivariograms were generated, and theoretical semivariogram parameters were obtained from a least-squares fit [42]. The root mean squared errors between the theoretical semivariogram and the experimental semivariogram were computed to determine the best suited model for a given DEM. Table I shows the derived values of the best fit semivariogram parameters for the data sets. In addition, the fitted semivariograms are plotted along with the experimentally derived semivariograms in Fig. 5.

From these results, one can see that the spherical theoretical model is a better fit for the smooth surface cases (roughness level 3), while the exponential model better fits the rougher surface samples. This is likely due to the fact that the exponential model tends to rise more steeply at short-scale lag distances, which corresponds well to the randomly distributed microfacets of the soil clods of our samples.

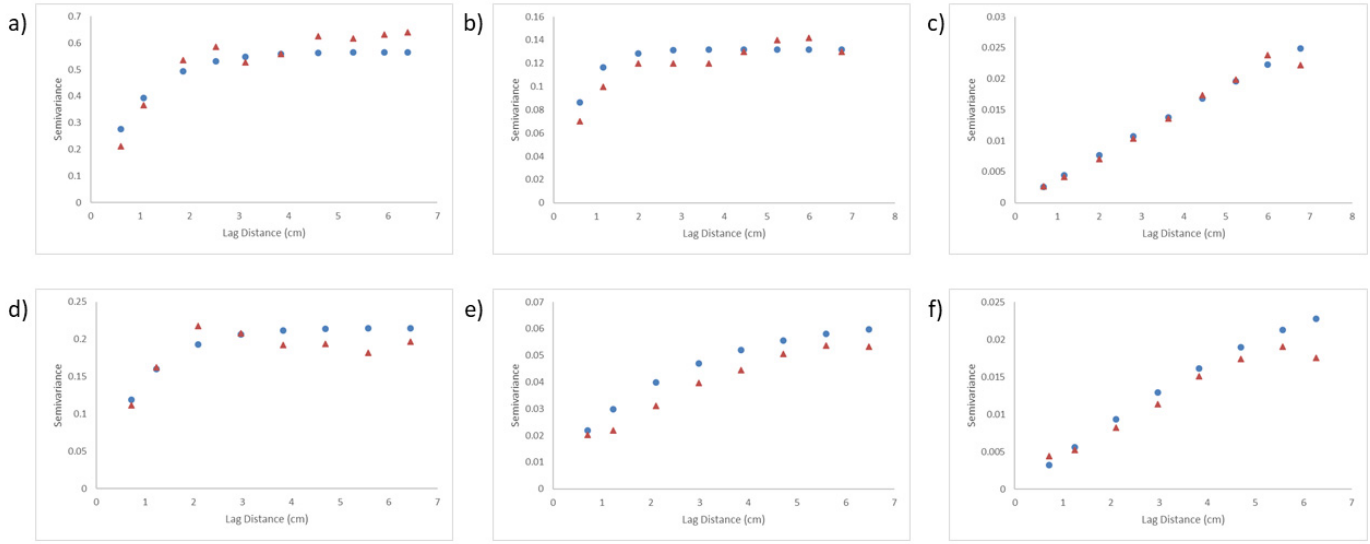

Fig. 5. Fitted theoretical semivariograms (blue circles) and experimentally measured semivariograms (red triangles) for the samples explored in this paper. Samples shown are (a)–(c) WA02-03 and (d)–(f) WA04-02 at roughness levels R1, R2, and R3, respectively.

TABLE I

ROUGHNESS METRICS OBTAINED FROM POSTPROCESSING OF DEM DATA: THE RANDOM ROUGHNESS METRIC AND THE OPTIMAL FITTED SEMIVARIOGRAM PARAMETERS THAT WERE OBTAINED AS A RESULT OF POSTPROCESSING THE DEM DATA OF THE SAMPLES

Sample	Roughness Level	Optimal Variogram Model	Sill Range (cm)	Sill Variance (cm^2)	Random Roughness, RR (cm^2)
WA02-03	1	Exponential	0.894	0.566	0.76
	2	Exponential	0.562	0.124	0.368
	3	Spherical	18.549	0.047	0.16
WA04-02	1	Exponential	0.922	0.214	0.461
	2	Exponential	3.206	0.062	0.226
	3	Spherical	7.979	0.028	0.124

We found a linear relationship between the fitted sill variance (SS) values and the corresponding random roughness values ($SS = 0.836 \times RR - 0.117$, $R^2 = 0.9407$). This relationship agrees with the published results that link the RR metric to sill variance metrics [4]. Both the metrics correspond to a breakdown in soil clods, as is expected. The limitation of the random RR metric is that it only provides information on the vertical component of roughness variation. Due to this limitation, information about how surface structure is correlated in the horizontal direction is ignored. In contrast, the fitted semivariogram model provides a measure for how both low and high spatial-frequency trends manifest themselves in the elevation measurements. This is described by the form of the sill range metric, which is the distance at which the sill variance is achieved; the value of the sill range is the spatial distance at which elevation measurements are no longer correlated with each other [31]. In this manner, the impact on surface RR calculations of cavities in between soil clods is partially accounted for by the sill variance metric.

IV. SPECTRAL ANALYSIS

In this section, we outline the routines developed to perform a spectral analysis on the clay samples used in this paper. This section focuses on correlating observed spectral metrics with the derived roughness metrics for each sample. We incorporate the 203 different measurement directions for each sample by calculating the variance in the band depth as a function of wavelength over all angular positions. In this sense, the directions outside of the plane are incorporated into all of the retrieved spectral metrics in this section.

A. Continuum Removal Over Entire Spectral Domain

We performed continuum removal over the reflectance spectrum of the measurements obtained at each respective sensor orientation of the BRF scan. We then examined the continuum-removed spectra as a function of wavelength in order to determine a qualitative trend between the variance of the continuum-removed spectra and the sample's state of macroscopic roughness. Renderings of the spectral measurements for the BRF measurements obtained for sediment sample WA04-02 are shown in Figs. 6 and 7.

Our results show that there is a clear decrease in the variance of the continuum-removed spectra as the sample becomes progressively smoother. This trend appears to hold over both oblique illumination conditions with a greater degree of single scattering, as well as for illumination conditions close to nadir where there is increased multiple scattering among or within surface cavities of the soil clods. However, the trend is far stronger for the BRF scans of the samples when the light source was oriented at the more oblique orientation of 45° zenith angle. The 45° light illumination configuration is associated with pronounced single scattering

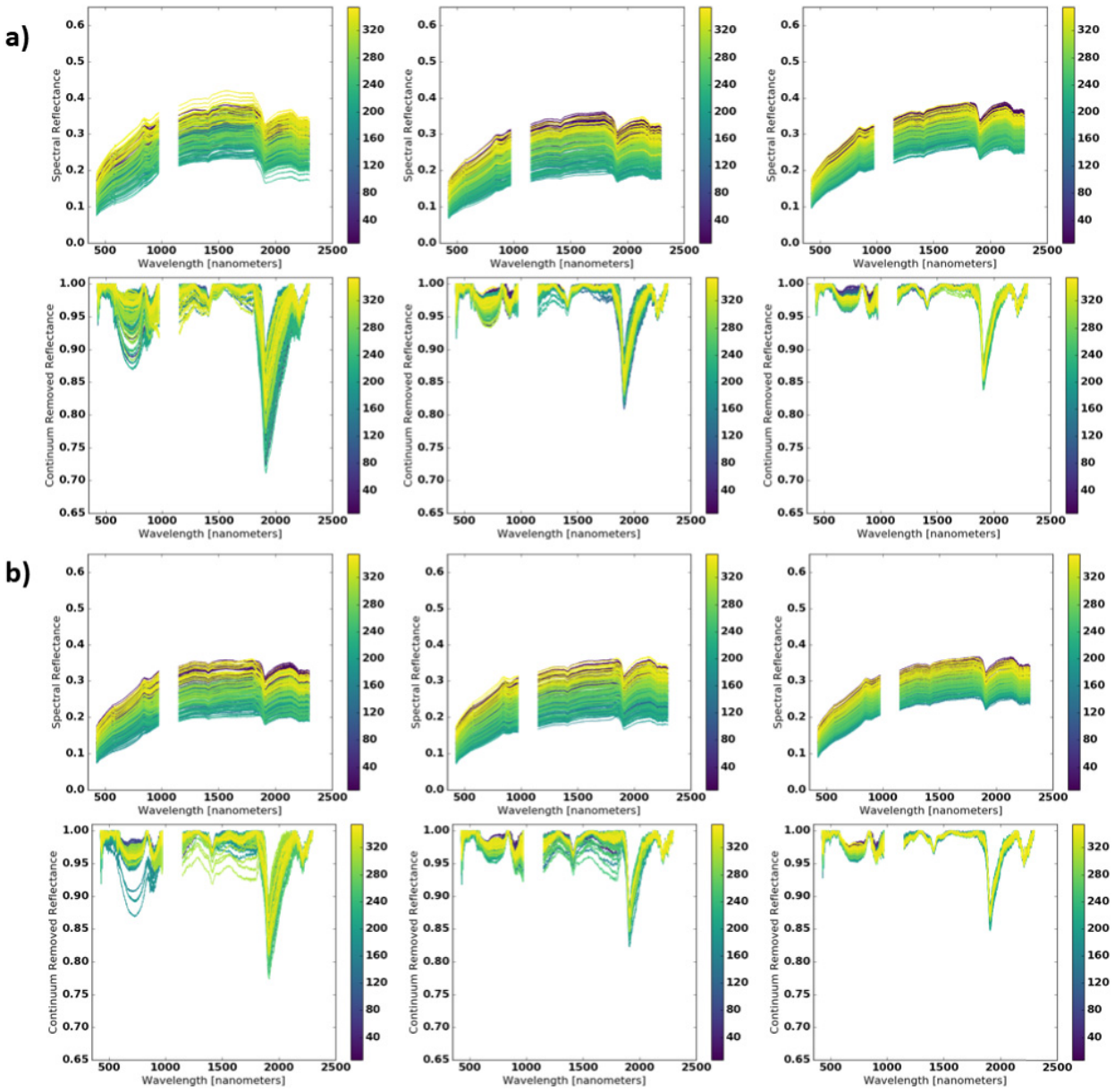

Fig. 6. Continuum removal performed on the reflectance spectrum of each sensor orientation of the BRF scan for sample WA04-02. (Top row) Spectral library rendering for each roughness state. (Bottom row) Corresponding output of the continuum-removal procedure. The macroscopic roughness of the sample of interest decreases from left to right. Renderings are shown for (a) light zenith angle of 25° and 5° fore-optic and (b) light zenith angle of 25° and 8° fore-optic.

and increased shadowing in the forward scattering directions from the sample.

It is also observed that there is a clear dependence on the sensor fore-optic attachment chosen for directional BRF measurements. While the relationship between variance in the continuum-removed spectra and the roughness state of the sample is still discernible for scans obtained using the 8° fore-optic, the trend is far more evident for scans obtained using the 5° fore-optic. This is observed in the measurements obtained for sample WA04-02 while the light was oriented at a 45° zenith angle as shown in Fig. 7.

As the sample was mechanically pulverized into a smoother state, the variance in the continuum-removed spectra was observed to decrease across almost all wavelengths. However, there were several regions of the sampled spectral range that were more greatly affected than others. In this paper, absorption features centered at approximately 590, 900, 1400, and 1910 nm were present in both the samples. Of these diagnostic features, the ones that were centered at approximately 900 and 1910 nm were the strongest across all BRF scans, and the variance of the continuum-removed spectra was strongest within these regions. We examine this relationship in a more quantitative manner in Sections IV-B and IV-C using convex hull calculations performed over the wings of the absorption feature.

Surprisingly, several spectral regions that were not identified by diagnostic absorption features also exhibited very strong variance in the continuum-removed reflectance. One such

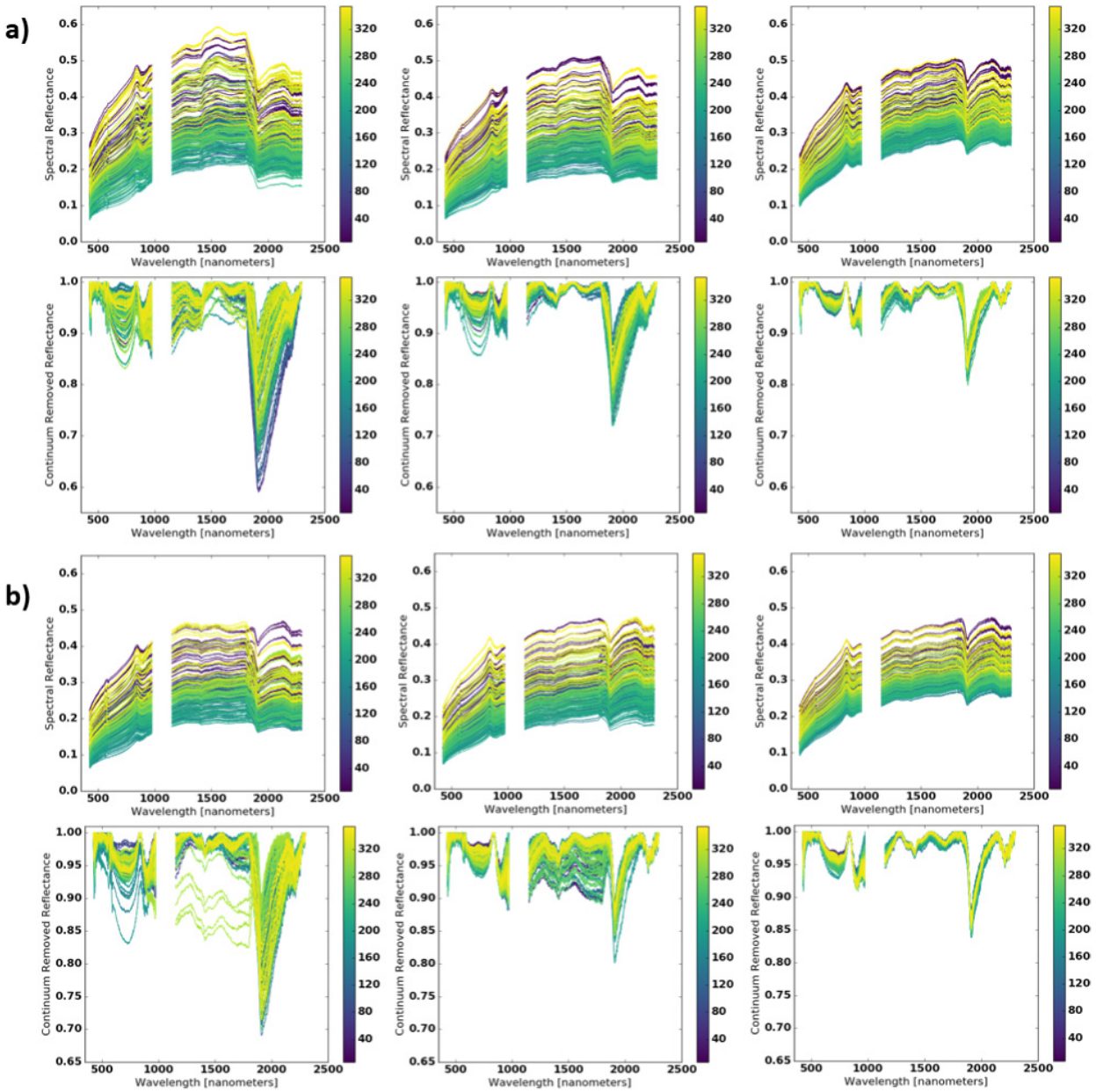

Fig. 7. Continuum removal performed on the reflectance spectrum of each sensor orientation of the BRF measurement for sample WA04-02. (Top row) Spectral library rendering for each roughness state. (Bottom row) Corresponding output of the continuum-removal procedure. The macroscopic roughness of the sample of interest decreases from left to right. Renderings are shown for (a) light zenith angle of 45° and 5° fore-optic and (b) light zenith angle of 45° and 8° fore-optic.

region occurred in the red to near-infrared region over a broad range of approximately 250 nm from approximately 600 to 850 nm. To obtain quantitative results, we also performed continuum removal using convex hull calculations within this spectral region.

B. Continuum Removal Over Determined Spectral Range

Continuum removal can be performed within spectral absorption features by selecting two predetermined wavelengths on the wings of a known diagnostic absorption feature and calculating the convex hull between these wavelengths. The two samples examined in this paper, WA02-03 and WA04-02, were collected at field sites that were relatively close geographically. The samples, therefore, had similar material properties and absorption features. Two absorption features that are characteristic of silty/clay soils were examined in this paper, approximately centered at wavelengths 900 and 1910 nm. We chose these regions, because both the materials exhibited absorption features in these spectral regions. For the continuum-removal procedure, the wavelength ranges chosen for convex hull calculations were 850–950 nm and 1870–2050 nm, respectively. We examined the depth and shapes of these absorption features across varying sensor viewing orientations to determine how macroscopic surface roughness correlated with variance in the spectral regions.

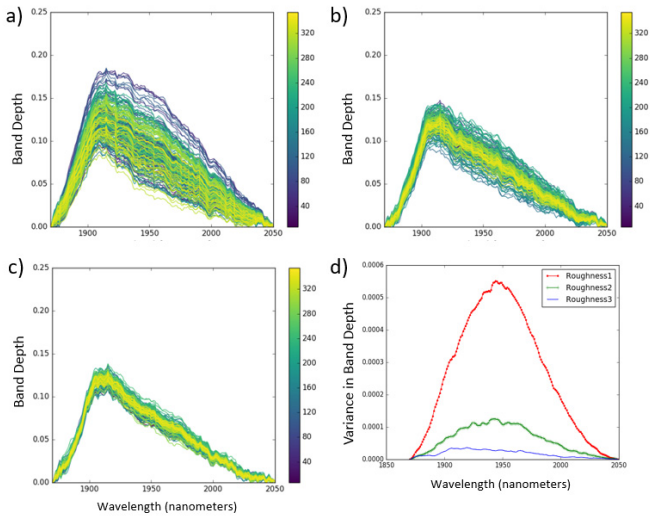

Fig. 8. Renderings of the band depths of the absorption feature centered around 1910 nm after performing continuum removal on the spectra shown in Fig. 6. (a)–(c) Roughness levels R1, R2, and R3, respectively. The color bar shows the azimuth angle corresponding to each sensor orientation of the BRF scan. The y-axis indicates the band depth at the respective wavelength. (d) Wavelength-dependent variance of the band depth plotted for these three roughness states.

Identifying this trend could provide evidence that determining roughness parameters within photometric models can be improved by examining the spectral domain. These diagnostic features will be discussed individually in Sections IV-B1 and IV-B2.

1) 1910-nm Absorption Feature: Both the samples examined in this paper had high concentrations of silt and clay and exhibited a strong absorption feature in the region of approximately 1910 nm that indicated the presence of a hydroxyl that has been adsorbed onto the grains of the soil [43]. We applied continuum removal across this diagnostic absorption feature using wavelengths located at 1870 and 2050 nm. The spectral library renderings of the BRF scans show a significant variation in both the band depth and the shape. An example of this appears in Fig. 7(a), which details the reflectance scans of sample WA04-02 while using a 5° fore-optic attachment and illuminating the sample at a 45° zenith angle. A color bar is included, showing the azimuth orientation of the fore-optic sensor for each respective measurement of the BRF scan.

By examining the spectral feature located around 1900 nm in Fig. 7(a), it is clear that there is a trend toward decreasing the variance of the band shape as the sample is progressively smoothed. The left wing of the absorption band gradually becomes less pronounced and eventually becomes symmetric with the right wing of the absorption band for the smoothest state of the material. In order to capture this trend quantitatively, we performed continuum removal on the absorption band for each sensor orientation of the BRF scan. The result of performing this procedure is shown in Fig. 8.

The band depth renderings shown in Fig. 8 show that, in general, the slope and magnitude of the right wing of the absorption feature exhibit a higher variance as the surface becomes progressively rougher. The variance of the left shoulder also increases but not as dramatically. In order to capture this trend, the wavelength-dependent variance of the band depth was calculated for each roughness state of a given sample, as shown in Fig. 8(d). It is evident that there is an increase in the variance of the band depth as the macroscopic roughness of the surface increases.

These results show that there is a clear correlation between the roughness level of a given sample and the variance in the wavelength-dependent band depth. In particular, for the curves shown in Fig. 8, there is a broad spectral range along the right wing of the absorption feature from approximately 1930 to 2000 nm where the relationship is the strongest. It should be noted that this trend holds across both the samples for all the combinations of fore-optic and light zenith angles. As a metric, we used the total variance within the absorption feature, calculated by performing numerical integration over the entire spectral range of the band-depth variance curves. We then correlated this metric, the total integrated variance, against the roughness metrics obtained using our elevation measurement system in this paper.

We carried out this procedure for both the samples that were used in this series of experiments (WA04-02 and WA02-03) and for all combinations of fore-optics (5° and 8°) and light zenith angles (25° and 45°). The fitted R^2 values obtained as a result of following this procedure for each measurement configuration appear in Table II.

A few observations can be made from Table II. There is a high correlation for the retrieved random-roughness metrics for both the samples across all measurement configurations ($R^2 \geq 0.97$). The sill variance metric has high correlation values for sample WA04-02 ($R^2 = 1.0$) but lower correlation values for sample WA02-03 ($R^2 \geq 0.85$). The process by which the theoretical semivariogram parameters are derived offers a potential explanation for this difference. Chiles and Delfiners [31] stated that the first few points of the experimental semivariogram are the most important for theoretical variogram fitting due to the fact that short-range points are used to model both the nugget variance and the slope at the origin. In particular, the nugget variance is a combination of factors, such as measurement noise, short-range trends, and microstructures, below the scale of the elevation measurement sampling. The most reliable solution for improving these estimates is to have a finer scale sampling grid for estimating the empirical semivariogram at short lag distances. This can be viewed as a critical next step for modeling the roughness of grains that vary on a subcentimeter scale.

2) 900-nm Absorption Feature: We applied the same approach described in Section IV-B1 to a spectral absorption feature in the region near 900 nm. To determine the convex hull for this absorption feature, we chose the spectral region from 850 to 950 nm. This absorption feature was much shallower than the one present at 1910 nm. An earlier study found that shallow absorption features can lead to difficulties in determining band depths accurately [12]. The continuum-removal analysis showed that the shallow nature of the absorption feature resulted in a greater noise when measuring both the samples WA04-02 and WA02-03. Nevertheless, for lighting conditions where the light was oriented at the 45° zenith angle, we still obtained a good correlation between the integrated

TABLE II

DERIVED R^2 VALUES FOR CORRELATIONS BETWEEN TOTAL INTEGRATED VARIANCE OF THE CONTINUUM REMOVED ABSORPTION FEATURE CENTERED AT 1910 NM AND THE ROUGHNESS METRICS USED IN THIS PAPER FOR SAMPLES WA02-03 AND WA04-02: FOR LIGHT ZENITH ANGLES OF 25° AND 45°

Sample	Roughness Metric	R^2 - 5 ° FoV, 25 ° Zenith	R^2 - 8° FoV, 25 ° Zenith	R^2 - 5° FoV, 45 ° Zenith	R^2 - 8° FoV, 45° Zenith
WA02-03	Random Roughness	1.00	0.97	0.98	1.00
	Sill Variance	0.95	0.85	0.88	0.93
WA04-02	Random Roughness	0.98	0.99	0.98	0.97
	Sill Variance	1.00	1.00	1.00	1.00

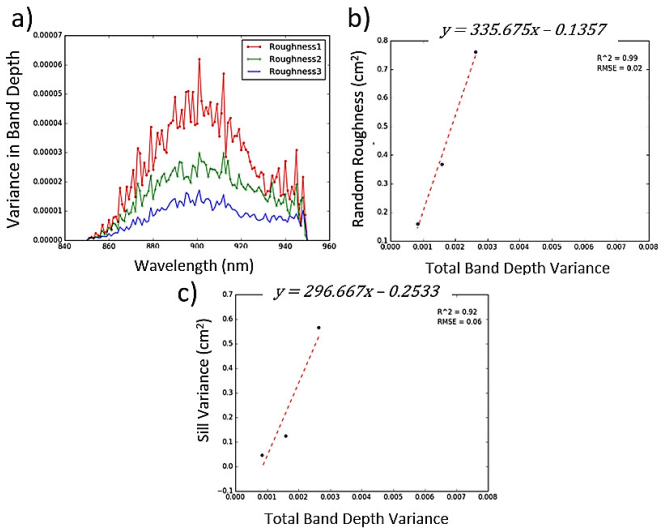

Fig. 9. (a) Variance in band depth for an absorption band centered at 900 nm for sample WA02-03 for the different roughness states. The light was positioned at a 45° zenith angle and a 5° fore-optic was used. Correlations between the total integrated variance and the roughness metrics used in this paper are shown for (b) random roughness and (c) sill variance.

wavelength-dependent variance of the band depth and the roughness state. For example, Fig. 9(a) shows the results obtained from the BRF measurements of sample WA02-03 while the light was oriented at a 45° zenith angle and a 5° fore-optic was used. The total integrated variance of the band depth and the roughness metrics used in this paper still exhibit a high degree of correlation as is shown in Fig. 9(b)–(d).

The result shown in Fig. 9 is an example of a case that is not corrupted by signal-to-noise issues, and often the trend between the total integrated variance and the roughness metrics for the absorption band was either not as obvious or somewhat reduced due to noise. This can potentially be attributed to the shallow depth of the absorption feature in comparison with the noise present in the corresponding spectral region. This is shown in Fig. 10, which shows results for several different BRF measurements performed in this paper.

C. Continuum Removal Outside of Absorption Bands

When we performed continuum removal over the entire reflectance spectrum, we observed that the variance within the spectral regions outside of diagnostic absorption features exhibited significant dependence on sensor orientation. One such spectral region was located between absorption features centered at 575 and 900 nm. Qualitatively, it can be seen that there is a significant variation of the slopes and convexity of this region depending on the view orientation of the sensor throughout the BRF measurement. We examined this spectral region by applying the same techniques that are outlined in Section IV-B1, despite the fact that the region was not in a spectral absorption feature. In order to analyze this spectral region, we applied continuum removal over the spectral region from 600 to 840 nm, which was free of spectral absorption features. Table III details the correlations that were observed between the total integrated variance of the "band depth" within this spectral region and the various roughness metrics that were used in this paper.

The correlation between derived values for the RR metric and the total integrated variance within the spectral region is high across all sensor fore-optics and light orientations for both the samples used in this paper ($R^2 \geq 0.91$). This would appear to indicate that even using roughness metrics related only to the vertical variance of the surface elevation with no information about the autocorrelation structure of the surface can be of significant value in the radiometric analysis.

The derived values for the sill variance roughness metric shows the weakest correlation to the total integrated variance within the spectral region, but R^2 is still relatively high across all sensor fore-optic measurements and light orientations ($1.00 \geq R^2 \geq 0.76$). As described earlier, the reason that the sill variance shows that overall weaker correlations could be related to the limitation of centimeter-scale accuracy of our current DEMs. It is very possible that incorporating the subcentimeter surface structure could improve our correlation results for this metric.

D. Spectral Derivative Analysis of Apparent Absorption Feature at 575 nm

A spectral absorption feature centered at approximately 575 nm was observed in the reflectance spectra of both the samples used in this paper. This feature was relatively weak and had an indeterminate band shape that varied with sensor orientation. Studies have also shown that noise in relatively weak absorption features can shift the apparent band centers significantly from their true position, which can hinder the ability to reliably determine the wings of a Gaussian-shaped absorption band [12]. For these reasons, we did not use a continuum-removal approach to investigate the dependence of the properties of this absorption on macroscopic surface roughness. Instead, we used a derivative analysis approach to investigate how this diagnostic feature behaved as the macroscopic roughness of the sample was altered. We observed that the average width of this spectral absorption feature in the

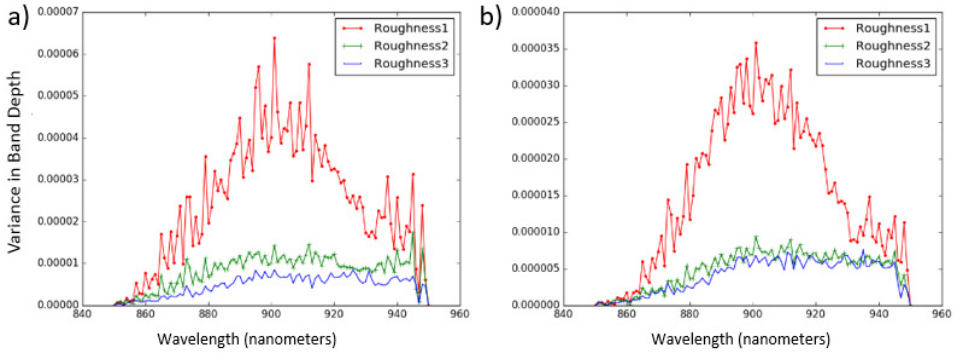

Fig. 10. Variance in band depths for 900-nm absorption feature. Scans shown are (a) WA02-03 with the light at 45° zenith angle and 8° fore-optic and (b) WA02-03 with the light at 25° and 8° fore-optic.

TABLE III

DERIVED R^2 VALUES FOR CORRELATIONS BETWEEN TOTAL INTEGRATED VARIANCE OF THE CONTINUUM REMOVED SPECTRAL REGION OF 600–850 NM THAT IS OUTSIDE OF SPECTRAL ABSORPTION FEATURES AND THE ROUGHNESS METRICS USED IN THIS PAPER FOR SAMPLES WA02-03 AND WA04-02: FOR LIGHT ZENITH ANGLES OF 25° AND 45°

Sample	Roughness Metric	R^2 - 5 ° FoV, 25 ° Zenith	R^2 - 8° FoV, 25 ° Zenith	R^2 - 5° FoV, 45 ° Zenith	R^2 - 8° FoV, 45° Zenith
WA02-03	Random Roughness	0.97	0.94	0.91	0.99
	Sill Variance	0.85	1.00	0.76	0.99
WA04-02	Random Roughness	0.99	0.95	0.98	0.93
	Sill Variance	1.00	0.88	1.00	0.85

BRF scans was approximately 15–20 nm, depending on the fore-optic used and the light zenith angle. We tested the band separation values of 5, 10, 15, and 20 nm to determine which provided the most reasonable results for the first- and second-order derivatives. We found that the band separation value of $\Delta\lambda = 10$-nm best mitigated spectral noise in the region of the absorption band, while at the same time providing an enhancement in the detection of the absorption feature.

In general, this spectral feature was strongest for rough surface conditions and illumination configurations with less diffused multiple scatter in the medium (i.e., at greater illumination zenith angles of the light source). Specifically, while we could resolve the absorption feature when the light was positioned close to nadir, the effect was most apparent when the illumination source was oriented at a zenith angle of 45°. The focus of the current discussion will be on cases where the light was positioned at an illumination zenith angle of 45°.

For both the samples, using the first- and second-order derivatives was more successful in detecting the absorption feature for configurations where the surface was macroscopically rough as opposed to smooth. The representative example shown in Fig. 11 illustrates this point. This figure shows the results obtained for sample WA02-03, while the light was positioned at a 45° zenith angle.

The spectral derivative analysis shows clearly that the ability to detect the spectral absorption feature centered approximately in the spectral region at 575 nm improves with the roughness of the sample (roughness levels #1 and #2). The first-order spectral derivative shows a local maximum across almost all sensor orientations in this spectral region; however, the magnitude of the first-order derivative of the spectral absorption feature is significantly lower when observing from sensor orientations which are offset from the principal plane of the illumination source. The second-order derivative is a positive band with a local maximum near the center of the absorption feature. This trend is most prevalent for the roughest states of the samples but is somewhat obscured by noise for the smoothest state of the samples (i.e., roughness level #3). Multiple scattering among and within the cavities of rough surfaces of the samples increases the time spent within the sediment clods and offers a plausible explanation for the enhancement of the second derivative in the rougher states. The reflectance spectrum of a material is composed of two major contributions: specular and diffuse. The specular component is assumed to consist of light that is primarily reflected off of particle surfaces without entering into the depths of the material. The diffuse component consists of light that may or may not penetrate into the material before being multiple scattered back into the direction of the sensor. Therefore, this diffused component contains information regarding the absorption bands [12]. When the material is smooth, multiple scattering and time spent in the material diminish, and the spectrum consists mostly of a specular component.

Interestingly, by examining these features on a smaller scale, we can also see that there is significant variance in the shape and center of the absorption band depending on the sensor view geometry. Fig. 12, which shows a BRF measurement of roughness level #2 of sample WA04-02 obtained using a light source orientation of 45° zenith angle and a 5° sensor fore-optic, illustrates this point. In this example, for sensor orientations that are relatively close to the backscattering lobe, the shape of the spectral band partially resembles a doublet, while for sensor orientations that are offset from the principal plane, the band shape more closely resembles a Gaussian. This could provide evidence that the spectral absorption band is in the strong surface scattering region for

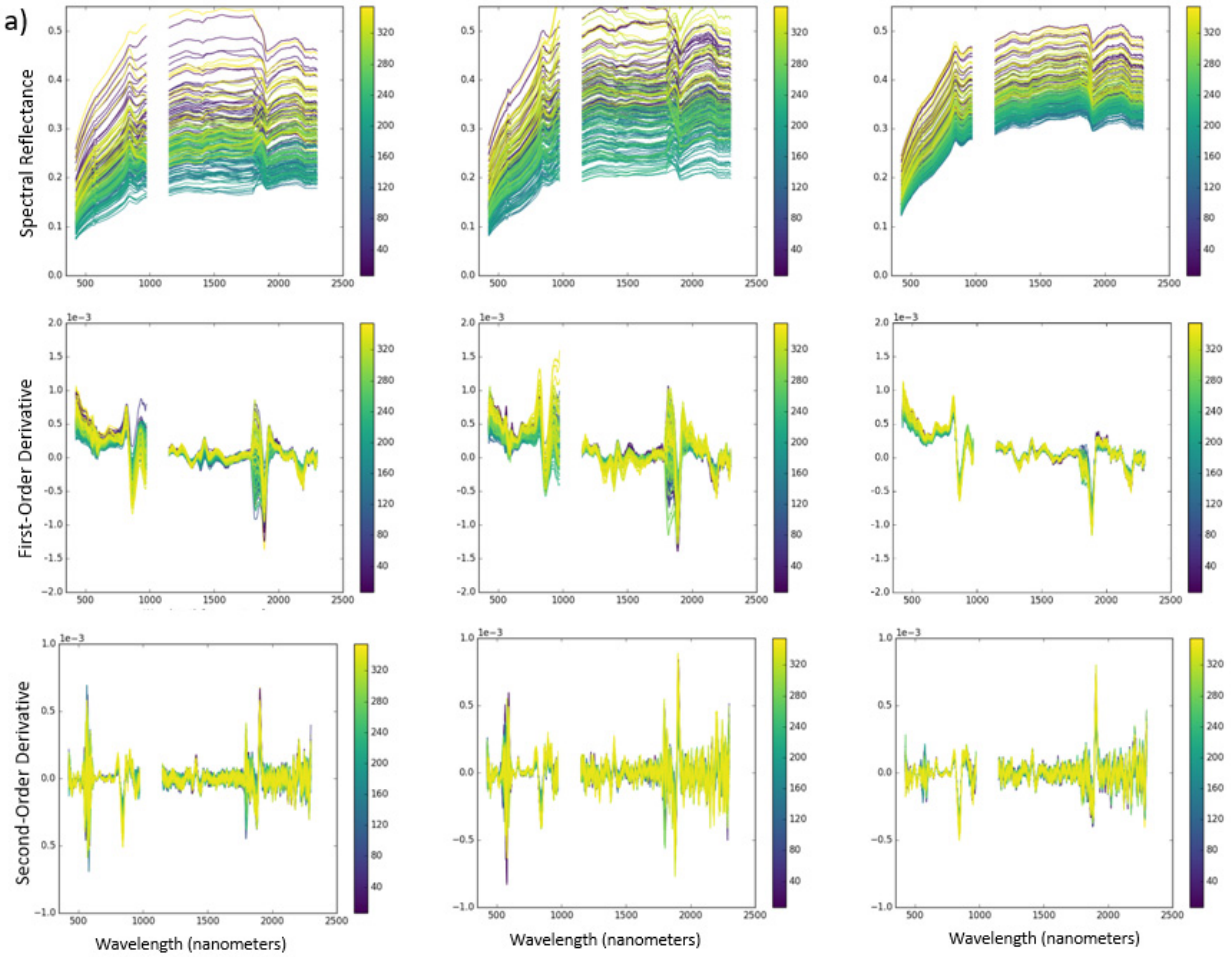

Fig. 11. Results obtained for sample WA02-03 while the light was oriented at a 45° zenith angle. The state of the material becomes smoother from left to right (roughness level 1: left-hand column and roughness level 3: right-hand column). (Top row) Spectral library after undergoing Savitsky–Golay smoothing. (Middle row) First-order spectral derivative. (Bottom row) Second-order spectral derivative. The results are shown for scans where the spectrometer attachment was a 5° fore-optic.

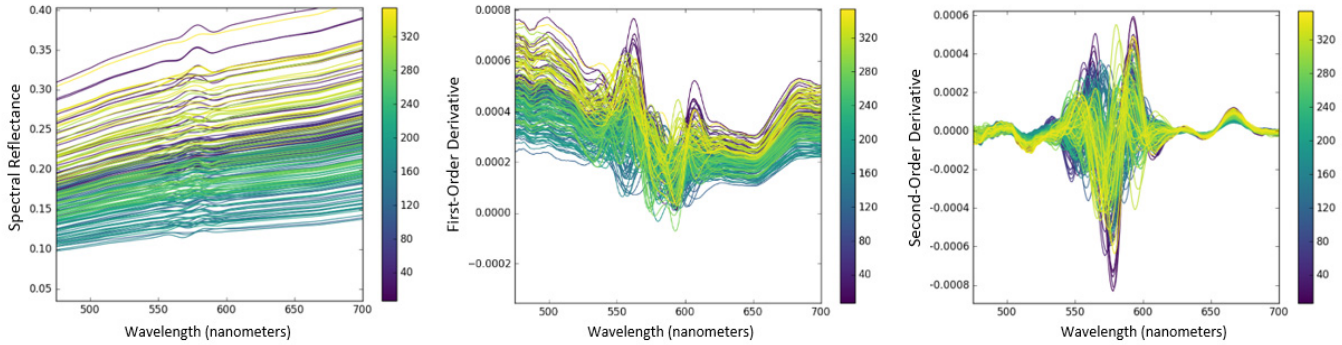

Fig. 12. Enlargement of the spectral region between 450 and 700 nm: results of a BRF scan of sample WA04-02, roughness state #2 obtained when the illumination source was at a 45° zenith angle and a 5° fore-optic was used on the spectrometer. From left to right: spectral library of the scan, first-order derivative, and second-order derivative.

the former case, and the volumetric scattering regime for the latter case, as is determined by the amount of time spent in the material [10]. By examining the spread of the local minimum across sensor orientations, we see that the first-order derivative exhibits a significant variance in the position of the band center. The second-order derivative, which conveys spectral curvature information, provides an evidence that the band shape is changing with the sensor orientation. A Gaussian absorption band shape should be reflected through its second-order derivative by having the appearance of a strongly positive band surrounded by two smaller negative bands on each side of it. The second-order derivative plots in Fig. 12 indicate

the presence of both the Gaussian and doublet band shapes present, depending on the sensor viewing geometry, and these shapes also appear in the original spectrum in Fig. 12.

V. Conclusion

The key finding of this paper is that the variance of spectral continuum-removed band depth integrated over relatively broad regions of the VNIR and SWIR portions of the spectrum can be used to obtain very good estimates of surface roughness. We found the strongest correlations in spectral regions that included an absorption feature; however, even outside of such features, correlations with well-established metrics of surface roughness were still very strong.

Results of this paper showed that the photometric effect of macroscopic surface roughness is sensitive to the size of the sensor field-of-view. We applied a method of continuum removal over the spectral region from 350 to 2500 nm for each respective sensor orientation angle of the BRF scan for each roughness level of the sediment. The result of this procedure showed that there was a discernible qualitative trend that the measurements obtained with the 5° fore-optic had considerably more variance in the spectral shape than the measurements obtained using the 8° fore-optic. This suggests that a smaller sensor solid-angle is considerably more sensitive to the effects of macroscopic surface roughness than larger sensor footprints. In future studies, we will investigate this trend for a wider range of sensor solid angles and for hyperspectral imagery acquired in field settings where a wider range of roughness scales is available. We performed a separate analysis of the data using spectral derivatives to investigate an alternative method of characterizing the appearance of a spectral absorption feature centered around 575 nm. We observed that with increasing roughness surfaces, i.e., when more surface cavities dominate the surface, the feature became significantly more well-defined. There was also a clear dependence of these effects on the sensor fore-optic. These results suggest that sensors possessing a larger field-of-view are less sensitive to the photometric effects of macroscopic surface roughness.

Another goal of this paper was to investigate the effect of macroscopic surface roughness when varying the zenith angle of the illumination source. In this paper, we contrasted illumination at a zenith angle close to nadir (25°), which provides a greater diffuse scattering, with illumination at an angle which offers less diffuse scattering (45°). The continuum-removal analysis showed that the spectral variance depended strongly on the illumination source orientation. In particular, this result was most evident when performing continuum removal within a spectral absorption band located in the spectral region around 1900 nm. The qualitative analysis showed that the variance in the band shape for rough samples within this spectral region was greater for measurements obtained while the light source was at a 45° zenith angle. Illuminating a rough surface from more oblique angles resulted in a greater single scattering from the surface, in which light can be reflected randomly by surface microfacets and may not be directed toward the sensor [10]. In addition, more oblique illumination conditions lead to a greater shadowing onto the sample in the forward scattering region of the sample's surface. On the other hand, nadir illumination conditions result in increased multiple scattering of light among and within cavities and consequently more time spent within the material before being reflected back to the sensor. This phenomenon could result in a more determinate band shape and band center due to a greater volume scattering [1].

The primary goal of this paper was to investigate the ability to correlate macroscopic surface roughness with roughness metrics derived from a custom laser range measurement system on our GRIT-T. Two different roughness metrics that are frequently utilized in the studies of macroscopic roughness were examined in this paper: the sill variance and the random roughness. These roughness metrics were highly correlated with a metric of variance in the band shape and the integrated band variance in a spectral region, for a spectral absorption feature located at 1900 nm. The results showed that for both the samples and all the configurations of fore-optics and illumination zenith angles, there were relatively high R^2 values across all roughness metrics. For the random roughness metric, the R^2 values for 5° and 8° fore-optics ranged between 0.91–1.00 and 0.93–1.00, respectively. For the sill variance metric, R^2 values for the 5° and 8° fore-optics ranged between 0.76–1.00 and 0.85–1.00, respectively. These correlations indicate that centimeter-scale elevation models can be directly related to variance in the band shape.

In addition to studying view-angle-dependent variance in the band shape for spectral absorption features, we also investigated a spectral region where no spectral absorption feature existed. This spectral region was in the near-infrared spectral region between 600 and 840 nm. We applied a continuum-removal procedure over this spectral range in order to obtain an estimate of the variance in the spectral shape as the roughness of the sample was varied. The correlation of roughness metrics with the total integrated variance in the band depth showed a strong relationship between increasing surface roughness and increasing spectral variance. For the random roughness metric, the R^2 values for a 5° fore-optic and 8° fore-optic ranged between 0.91–0.99 and 0.93–0.99, respectively. For the sill variance roughness metric, the R^2 values of 5° and 8° fore-optics ranged between 0.76–1.00 and 0.85–1.00, respectively. These results indicate that even spectrometers that are only capable of measuring in the visible and near-infrared spectral regions can provide insight into surface roughness properties.

References

[1] B. Hapke, "Bidirectional reflectance spectroscopy: 3. Correction for macroscopic roughness," *Icarus*, vol. 59, no. 1, pp. 41–59, Jul. 1984.

[2] M. K. Shepard and R. E. Arvidson, "The opposition surge and photopolarimetry of fresh and coated basalts," *Icarus*, vol. 141, no. 1, pp. 172–178, 1999. [Online]. Available: http://www.sciencedirect.com/science/article/pii/S001910359996150X

[3] M. K. Shepard and P. Helfenstein, "A laboratory study of the bidirectional reflectance from particulate samples," *Icarus*, vol. 215, no. 2, pp. 526–533, Oct. 2011.

[4] H. Croft, K. Anderson, R. E. Brazier, and N. J. Kuhn, "Modeling fine-scale soil surface structure using geostatistics," *Water Resour. Res.*, vol. 49, no. 4, pp. 1858–1870, Apr. 2013.

[5] Z. Wang, C. A. Coburn, X. Ren, and P. M. Teillet, "Effect of surface roughness, wavelength, illumination, and viewing zenith angles on soil surface BRDF using an imaging BRDF approach," *Int. J. Remote Sens.*, vol. 35, no. 19, pp. 6894–6913, 2014. [Online]. Available: http://www.tandfonline.com/doi/abs/10.1080/01431161.2014.960616

[6] C. M. Bachmann *et al.*, "A flexible field goniometer system: The Goniometer for outdoor portable hyperspectral Earth reflectance," *J. Appl. Remote Sens.*, vol. 10, no. 3, Aug. 2016, Art. no. 036012.
[7] H. Croft, K. Anderson, and N. J. Kuhn, "Reflectance anisotropy for measuring soil surface roughness of multiple soil types," *CATENA*, vol. 93, pp. 87–96, Jun. 2012.
[8] H. Croft, K. Anderson, and N. J. Kuhn, "Evaluating the influence of surface soil moisture and soil surface roughness on optical directional reflectance factors," *Eur. J. Soil Sci.*, vol. 65, no. 4, pp. 605–612, Jul. 2014.
[9] R. N. Clark and T. L. Roush, "Reflectance spectroscopy: Quantitative analysis techniques for remote sensing applications," *J. Geophys. Res.*, vol. 89, no. B7, pp. 6329–6340, Jul. 1984.
[10] B. Hapke, *Theory of Reflectance and Emittance Spectroscopy*. Cambridge, U.K.: Cambridge Univ. Press, 2012.
[11] M. T. Eismann, *Hyperspectral Remote Sensing*. Bellingham, WA, USA: SPIE, 2012.
[12] R. L. Huguenin and J. L. Jones, "Intelligent information extraction from reflectance spectra: Absorption band positions," *J. Geophys. Res.*, vol. 91, no. B9, pp. 9585–9598, Aug. 1986.
[13] J. R. Schott, *Remote Sensing: The Image Chain Approach*, 2nd ed. New York, NY, USA: Oxford Univ. Press, 2007.
[14] J. D. Harms, C. M. Bachmann, J. W. Faulring, and A. J. R. Torres, "A next generation field-portable goniometer system," *Proc. SPIE*, vol. 9840, May 2016, Art. no. 98400J.
[15] J. D. Harms *et al.*, "Fully automated laboratory and field-portable goniometer used for performing accurate and precise multiangular reflectance measurements," *J. Appl. Remote Sens.*, vol. 11, no. 4, Nov. 2017, Art. no. 046014.
[16] H. Zhang, K. J. Voss, R. P. Reid, and E. M. Louchard, "Bidirectional reflectance measurements of sediments in the vicinity of lee stocking Island, Bahamas," *Limnol. Oceanogr.*, vol. 48, no. 1, pp. 380–389, Jan. 2003.
[17] G. S. Okin and T. H. Painter, "Effect of grain size on remotely sensed spectral reflectance of sandy desert surfaces," *Remote Sens. Environ.*, vol. 89, no. 3, pp. 272–280, Feb. 2004.
[18] Y. Lv and Z. Sun, "Multi-angular spectral reflectance to characterize the particle size of surfaces of desert and cultivated soil," *Eur. J. Soil Sci.*, vol. 67, no. 3, pp. 253–265, May 2016.
[19] Z. Sun, Y. Lv, and Z. Tong, "Effects of particle size on bidirectional reflectance factor measurements from particulate surfaces," *Opt. Express*, vol. 24, no. 6, pp. A612–A634, 2016.
[20] C. M. Bachmann, R. S. Eon, B. Ambeau, J. Harms, G. Badura, and C. Griffo, "Modeling and intercomparison of field and laboratory hyperspectral goniometer measurements with G-LIHT imagery of the algodones dunes," *J. Appl. Remote Sens.*, vol. 12, no. 1, Sep. 2017, Art. no. 012005.
[21] R. S. Eon, C. M. Bachmann, and A. D. Gerace, "Retrieval of sediment fill factor by inversion of a modified Hapke model applied to sampled HCRF from airborne and satellite imagery," *Remote Sens.*, vol. 10, no. 11, p. 1758, Nov. 2018.
[22] J. Cierniewski and M. Gulinski, "Furrow microrelief influence on the directional hyperspectral reflectance of soil at various illumination and observation conditions," *IEEE Trans. Geosci. Remote Sens.*, vol. 48, no. 11, pp. 4143–4148, Nov. 2010.
[23] G. S. Okin, B. Murray, and W. H. Schlesinger, "Degradation of sandy arid shrubland environments: observations, process modelling, and management implications," *J. Arid Environ.*, vol. 47, no. 2, pp. 123–144, Feb. 2001.
[24] A. Chappell, T. M. Zobeck, and G. Brunner, "Using bi-directional soil spectral reflectance to model soil surface changes induced by rainfall and wind-tunnel abrasion," *Remote Sens. Environ.*, vol. 102, nos. 3–4, pp. 328–343, Jun. 2006.
[25] A. Chappell, C. Strong, G. McTainsh, and J. Leys, "Detecting induced in situ erodibility of a dust-producing playa in Australia using a bi-directional soil spectral reflectance model," *Remote Sens. Environ.*, vol. 106, no. 4, pp. 508–524, 2007.
[26] A. Chappell, S. Van Pelt, T. Zobeck, and Z. Dong, "Estimating aerodynamic resistance of rough surfaces using angular reflectance," *Remote Sens. Environ.*, vol. 114, no. 7, pp. 1462–1470, 2010.
[27] E. Ben-Dor *et al.*, "Using imaging spectroscopy to study soil properties," *Remote Sens. Environ.*, vol. 113, pp. S38–S55, Sep. 2009.
[28] F. E. Nicodemus, J. C. Richmond, and J. J. Hsia, *Geometrical Considerations Nomenclature for Reflectance*, vol. 160. Gaithersburg, MD, USA: Nat. Bur. Standards, 1977.
[29] G. Schaepman-Strub, M. E. Schaepman, T. H. Painter, S. Dangel, and J. V. Martonchik, "Reflectance quantities in optical remote sensing—Definitions and case studies," *Remote Sens. Environ.*, vol. 103, no. 1, pp. 27–42, 2006.
[30] E. J. Milton, "Review article principles of field spectroscopy," *Remote Sens.*, vol. 8, no. 12, pp. 1807–1827, 1987.
[31] J.-P. Chilès and P. Delfiner, "Geostatistics: Modeling spatial uncertainty," in *Wiley Series in Probability and Statistics Book*, vol. 713. New York, NY, USA: Wiley, 1999, p. 695.
[32] N. A. Cressie, *Statistics for Spatial Data*, vol. 14. Hoboken, NJ, USA: Wiley, 1993, pp. 547–550.
[33] M. A. Oliver and R. Webster, *Basic Steps in Geostatistics: The Variogram and Kriging*. New York, NY, USA: Springer, 2015.
[34] T. Hengl, *A Practical Guide to Geostatistical Mapping*. Amsterdam, The Netherlands: Hengl, 2009. [Online]. Available: http://book.spatial-analyst.net/system/files/cover_geostat_2009.pdf
[35] E. S. Anderson, J. A. Thompson, and R. E. Austin, "LIDAR density and linear interpolator effects on elevation estimates," *Int. J. Remote Sens.*, vol. 26, no. 18, pp. 3889–3900, 2005.
[36] D. L. Corwin, J. Hopmans, and G. H. de Rooij, "From field-to landscape-scale vadose zone processes: Scale issues, modeling, and monitoring," *Vadose Zone J.*, vol. 5, no. 1, pp. 129–139, Jan. 2006.
[37] H. Kuipers, "A relief meter for soil cumulative studies," *Netherlands J. Agricultural Sci.*, vol. 5, no. 4, pp. 255–262, Nov. 1957.
[38] F. Tsai and W. Philpot, "Derivative analysis of hyperspectral data," *Remote Sens. Environ.*, vol. 66, no. 1, pp. 41–51, Oct. 1998.
[39] A. Savitzky and M. J. E. Golay, "Smoothing and differentiation of data by simplified least squares procedures," *Analytical Chem.*, vol. 36, no. 8, pp. 1627–1639, 1964.
[40] Z. Huang, B. J. Turner, S. J. Dury, I. R. Wallis, and W. J. Foley, "Estimating foliage nitrogen concentration from HYMAP data using continuum removal analysis," *Remote Sens. Environ.*, vol. 93, nos. 1–2, pp. 18–29, Oct. 2004.
[41] R. F. Kokaly and R. N. Clark, "Spectroscopic determination of leaf biochemistry using band-depth analysis of absorption features and stepwise multiple linear regression," *Remote Sens. Environ.*, vol. 67, no. 3, pp. 267–287, Mar. 1999.
[42] E. J. Pebesma, "Multivariable geostatistics in S: The gstat package," *Comput. Geosci.*, vol. 30, pp. 683–691, Aug. 2004.
[43] R. J. Murphy, "Evaluating simple proxy measures for estimating depth of the $\sim$ 1900 nm water absorption feature from hyperspectral data acquired under natural illumination," *Remote Sens. Environ.*, vol. 166, pp. 22–33, Sep. 2015. doi: 10.1016/j.rse.2015.05.029.

Gregory Badura received the Ph.D. degree in imaging science from the Rochester Institute of Technology, Rochester, NY, USA, in 2018.

He is currently with the Georgia Tech Research Institute, Atlanta, GA, USA. His research interests include radiative transfer modeling of soils and vegetation, digital elevation model analysis, and hyperspectral image analysis.

Charles M. Bachmann received the A.B. degree in physics from Princeton University, Princeton, NJ, USA, in 1984, and the Sc.M. and Ph.D. degrees in physics from Brown University, Providence, RI, USA, in 1986 and 1990, respectively.

He was a Research Physicist with the U.S. Naval Research Laboratory, Washington, DC, USA, from 1990 to 2013, where he served as the Head of the Coastal Science and Interpretation Section, Remote Sensing Division, from 2003 to 2013. From 2012 to 2013, through the U.S. Navy Engineer and Scientist Exchange Program, he was with the Defense Science Technology Organization (DSTO) Maritime Division, Sydney, NSW, Australia. In 2013, he joined the Faculty of the Chester F. Carlson Center for Imaging Science (CIS), Rochester Institute of Technology (RIT), Rochester, NY, USA, as the Frederick and Anna B. Wiedman Chair, where he has been serving as the CIS Graduate Program Coordinator since 2016. He holds two U.S. patents for methods of analysis related to hyperspectral remote-sensing imagery. His research interests include hyperspectral remote sensing of coastal and desert environments, bidirectional reflectance factor and radiative transfer modeling for retrieval of geophysical and biophysical parameters, field calibration and validation, the development of advanced instrumentation (goniometers), and abstract models for interpreting hyperspectral and multisensor imagery based on manifold descriptions and graph theory.

Justin Harms, photograph and biography not available at the time of publication.

Andrei Abelev, photograph and biography not available at the time of publication.